

Enhanced ammonia sensing by Sn doped ZnO films prepared by a low-cost fully automated nebulizer spray technique

K. Ravichandran¹ · A. Manivasagam¹

Received: 1 November 2016 / Accepted: 28 December 2016 / Published online: 13 January 2017
© Springer Science+Business Media New York 2017

Abstract Sn doped ZnO (TZO) thin films were deposited using a homemade nebulizer spray pyrolysis unit on glass substrates. The Sn doping concentration in the starting solution is varied as 2, 4, 6 and 8 at.% and the effect of Sn doping level on the structural, optical, surface morphological and gas sensing properties were investigated. The XRD results reveal that all the films have polycrystalline nature with hexagonal wurtzite structure and the optical studies show that the average transmittance of the deposited films is about 80% in the visible region. All the films show good ammonia gas sensing behavior. Especially, ZnO:Sn film with 6 at.% of Sn doping shows the best response time and recovery time for ammonia gas sensing at room temperature. The AFM results reveal that at 6 at.% of Sn doping, the ZnO film shows maximum roughness and high porosity.

1 Introduction

Ammonia is one of the major raw materials used in various industries like chemicals, textiles, fertilizers, cosmetics, automobiles and paper product industries. More than 100 million tons of ammonia was produced every year for a wide range of utilities [1]. As a colorless gas with a pungent odor, ammonia is the major pollution content of soil and water which affects aquatic organisms and terrestrial plants [2]. Inhaling ammonia affects eye, nose, throat as well as skin, which can lead to vomiting, headache, pneumonia and

even death [3]. Hence, it is very important to sense as well as to monitor ammonia level in water, soil and to control leakage of ammonia gas in the atmosphere.

Design and development of low-cost gas sensors using reliable and promising materials for sensing ammonia pave a way for intense research in this field. ZnO, an n-type semiconductor oxide, is one of the most promising and frequently used sensing materials due to its low cost, flexible and tunable properties [4]. But, pristine ZnO exhibits poor response and recovery for ammonia gas [5, 6]. Suitable doping can result in enhanced sensing properties including sensitivity, repeatability and long-term stability. There are several suitable dopants like Fe, Co, F, Ni, Cu, Sn, Cr and Mo [7–10]. Of these elements, in this study, tin (Sn) is selected as a dopant to ZnO.

ZnO films have been prepared by various methods, including radio frequency sputtering, electron beam evaporation, pulsed laser deposition, chemical vapor deposition, nebulizer spray pyrolysis and sol–gel processing [11–17]. Of these techniques, nebulizer spray pyrolysis is simple and inexpensive and offers several other advantages for the deposition of doped TCO films [18]. In the present work, a simple Automated Jet Nebulizer Spray Technique (AJNST) is utilized to deposit tin doped zinc oxide films (TZO).

2 Materials and methods

2.1 Film deposition

The homemade AJNST coating unit employed in the present studies is shown in Fig. 1. The deposition parameters adopted are given in Table 1.

The precursor solution was prepared by dissolving required amount of zinc acetate dihydrate

✉ K. Ravichandran
kkrl365@yahoo.com; kkravi1365@gmail.com

¹ Materials Science Research Laboratory, PG and Research Department of Physics, AVVM Sri Pushpam College (Autonomous), Poondi, Thanjavur, Tamil Nadu 613 503, India

Fig. 1 Schematic diagram of automated jet nebulizer spray system

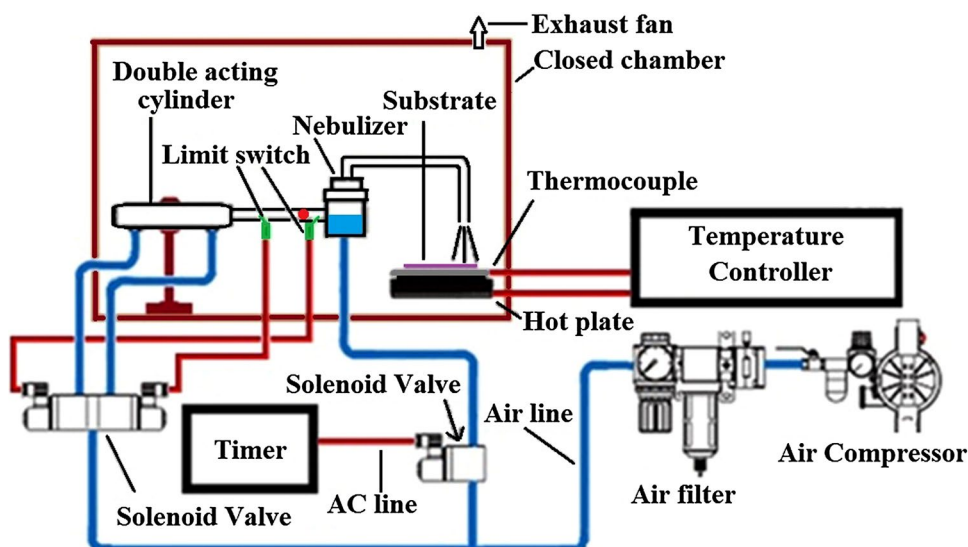


Table 1 Source materials and deposition parameters employed

Zinc acetate dihydrate (host precursor)	0.1 M
Tin (II) chloride penta hydrate (dopant precursor)	2, 4, 6 and 8 at. %
Spray nozzle diameter	10 mm
Flow rate	0.637 mL min ⁻¹
Carrier gas pressure	1.5 bar
Spray time	14 s
Time interval between successive sprays	8 s
Substrate–nozzle distance	10 cm
Substrate temperature	400 °C
Volume of precursor	20 mL

(Zn(CH₃COO)₂·2H₂O) and tin(II) chloride penta hydrate (SnCl₂·5H₂O) with the solvent comprising of doubly deionized water, methanol and acetic acid are in the ratio 7:2:1 to obtain 0.1 M of the starting solution. The jet nebulizer was filled with the precursor solution and pressurized by double filtered oil/moisture free compressed air to get a uniform deposition on the glass substrate. The jet nebulizer spray is mounted with the help of a stand and can be moved horizontally to cover a large area and to produce precisely controlled atomized coatings.

Microscope slides (Labtech medico (P) Ltd, Mumbai) which are used as substrates were cleaned properly with HCl, acetone and deionized water using an ultrasonic bath (Supersonics, Mumbai). The glass substrates were positioned on the hot plate in which the temperature was digitally controlled with a help of K type thermocouple on the surface of the heater. The spray tube–substrate distance was optimized to ensure that the pressurized mist reaches the hot substrate and decomposes to form a thin film. To facilitate the reproducibility, seven sets of samples were

prepared. A suitable amount of Sn is doped with ZnO such that dopant precursor (SnCl₂·5H₂O) concentrations in the starting solutions are 2, 4, 6 and 8 at.%. The respective samples are named as A1, A2, A3 and A4.

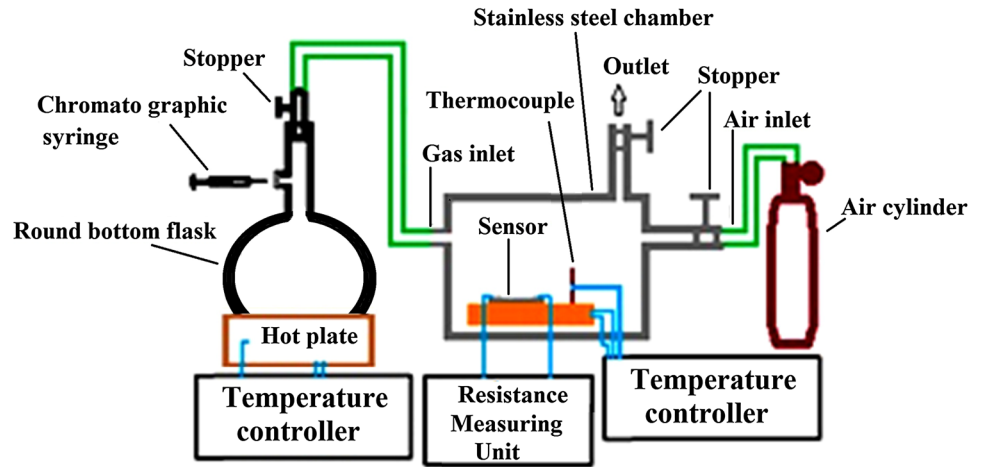
2.2 Film characterization

The structural properties of the films were studied using X-ray diffractometer (PAN analytical-PW 340/60 X' Pert PRO) with X-ray (Cu–K_α) of wavelength 1.5406 Å. A UV–vis–NIR double beam spectrophotometer (LAMBDA-35) was used to study the optical properties of the films in the wavelength range of 300–1100 nm. The thickness of the films was measured by means of both stylus technique (profilometer: Surf Test SJ-301) and weight gain method. The mean value of the sample thickness was found to be in the range of 450–600 nm. The electrical resistivity of the films was determined using four point probe technique with Vander Paw configuration. The film surface morphology was studied using FESEM (HITACHI S-3000 H) and Atomic Force microscopy (Veeco-di-CPII). Photoluminescence (PL) studies were carried out using a spectral-fluorometer (JobinYvon_FLUROLOG-FL3-11) with xenon lamp (450 W) as the source for the excitation wavelength of 325 nm.

2.3 Gas sensing arrangement

A stainless steel chamber, the schematic diagram of which is shown in Fig. 2 is used for gas sensing measurements. It consists of a substrate holder placed inside the chamber. Contacts were made at both ends of the samples with a resistance measuring unit using a silver paste. Chamber temperature was kept at constant and monitored by a

Fig. 2 Schematic diagram of the experimental setup used for gas sensing measurements



thermocouple and temperature controller. Chamber is connected to a round bottom flask of 2-liter capacity and a dry air cylinder. Ammonia solution was injected into the flask by chromatographic syringe and the gas is allowed to enter the chamber from the flask which interacts with the film and thereby changes the resistance of the film. By measuring the resistivity of the prepared samples with respect to gas concentration and time, we can calculate the sensing parameters of the samples. All sensing studies were made at room temperature and the sensing area was kept constant as 1.5 cm² for all the samples.

3 Result and discussion

3.1 X-ray diffraction

To investigate the crystalline nature and preferential orientation of TZO films, X-ray diffraction analysis was carried out. The XRD patterns are given in Fig. 3a. The diffraction peaks at the Bragg angles 31.7°, 34.4° and 36.3° corresponding to (100), (002) and (101), respectively, which confirm the hexagonal wurtzite structure of the samples. No secondary phases are detected related to Sn.

The crystallite size was calculated using Scherrer’s formula [19]

$$D = \frac{0.94\lambda}{\beta \cos \theta} \quad (1)$$

where, 0.94 is the shape factor, λ is the wavelength of X-rays (1.5406 Å), β is the full width at half maximum (FWHM) in radians, θ is the diffraction angle [20]. The calculated values are given in Table 2 and found to be in the range of 28 to 56 nm. The intensities of (100) and (002) planes increase for 4 at.% of Sn doping and then decrease for further increase in the Sn doping level. The

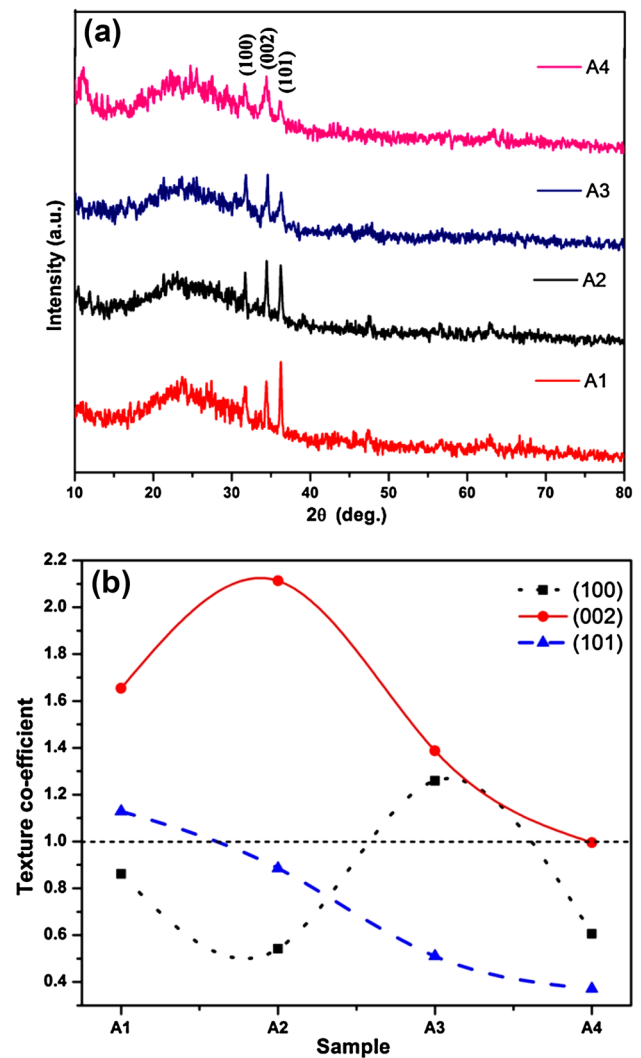


Fig. 3 a X-ray diffraction patterns and b variation in texture coefficient of the TZO films

Table 2 Structural parameters of TZO thin films

Name of the sample	Plane	a (Å)	c (Å)	D (nm)
A1	(002)	3.47	5.21	28
A2	(002)	3.47	5.21	56
A3	(002)	3.47	5.19	42
A4	(002)	3.75	5.65	14

Table 3 Texture coefficient of TZO films

Sample code	Texture coefficient (TC)		
	(100)	(002)	(101)
A1	0.86163	1.65416	1.12877
A2	0.54188	2.11312	0.88514
A3	1.25961	1.38762	0.51006
A4	0.60548	0.99525	0.37058

crystallite size decreases for further Sn doping which may be due to Zener pinning effect. Due to the difference in the ionic radii, as Sn percentage increases the lattice disorder increases [21]. The preferential/random growth of the crystallites can be understood from texture coefficient [TC(hkl)] values of the crystal planes.

The $TC_{(hkl)}$ values can be calculated using the following equation [22].

$$TC_{(hkl)} = \frac{I_{(hkl)}/I_{0(hkl)}}{(1/N) \sum_N (I_{(hkl)}/I_{0(hkl)})} \quad (2)$$

where $I_{(hkl)}$ and $I_{0(hkl)}$ are the observed and standard intensities, respectively, of the diffracted peaks related to (hkl) planes. N is the number of diffracted lines observed in the XRD pattern of a particular film (Fig. 3b). The calculated TC values are given in Table 3. It is observed that all the TZO films exhibit (002) preferred orientation. There is no change of preferential orientation which may be due to the

proper substitutional replacement of Zn ions by Sn ions in the ZnO matrix.

The lattice constants ‘a’ and ‘c’ are calculated using the relation (3) [23].

$$\frac{1}{d^2} = \frac{4}{3a^2} (h^2 + hk + k^2) + \frac{l^2}{c^2} \quad (3)$$

where, d is the interplanar distance and (hkl) is the Miller indices of the planes.

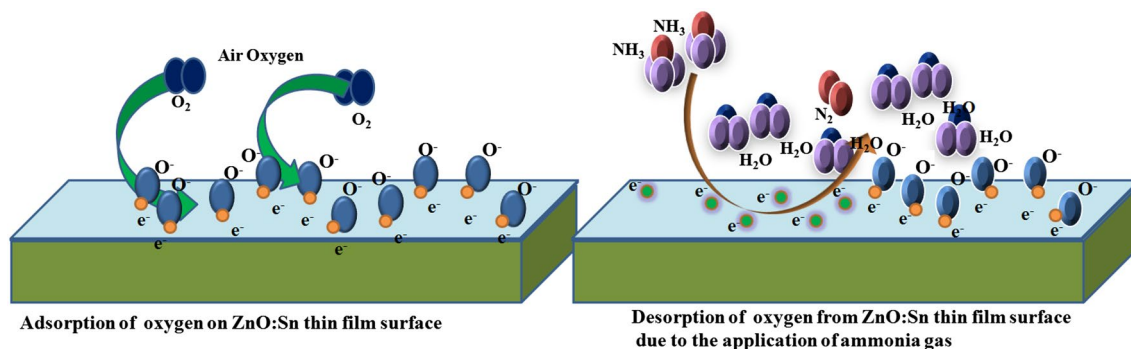
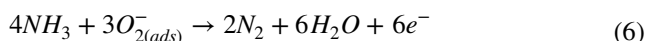
3.2 Gas sensing study

The deposited Sn doped ZnO (TZO) thin films are subjected to ammonia gas sensing. At room temperature, oxygen is adsorbed by the surface of the film from the atmosphere and the adsorbed oxygen acquires electrons from the conduction band of ZnO and forms oxygen ions (O_2^-) as represented by the Eq. (4) [24].



Oxygen ions, generated from this reaction leads to an increase in the resistance of the film. The maximum value of the resistance is denoted as “air resistance (R_a)” (also called as initial resistance or base resistance). When the ammonia gas was allowed to enter the chamber, the surface oxygen ions react with the ammonia gas to release free electrons which reduce the resistance of the film as shown in Fig. 4 [25]. The observed change in resistance with respect to time is shown in Fig. 5a–d. The gas detection mechanism is based on the surface reaction between the atmospheric oxygen and the applied gas. The resistance of the film decreases gradually with the inclusion of ammonia gas and reaches a minimum value called as gas resistance (R_g).

The following Eqs. (5) and (6) represent the overall reducing reaction [26].

**Fig. 4** Schematic diagram of oxygen adsorption and ammonia gas sensing mechanism

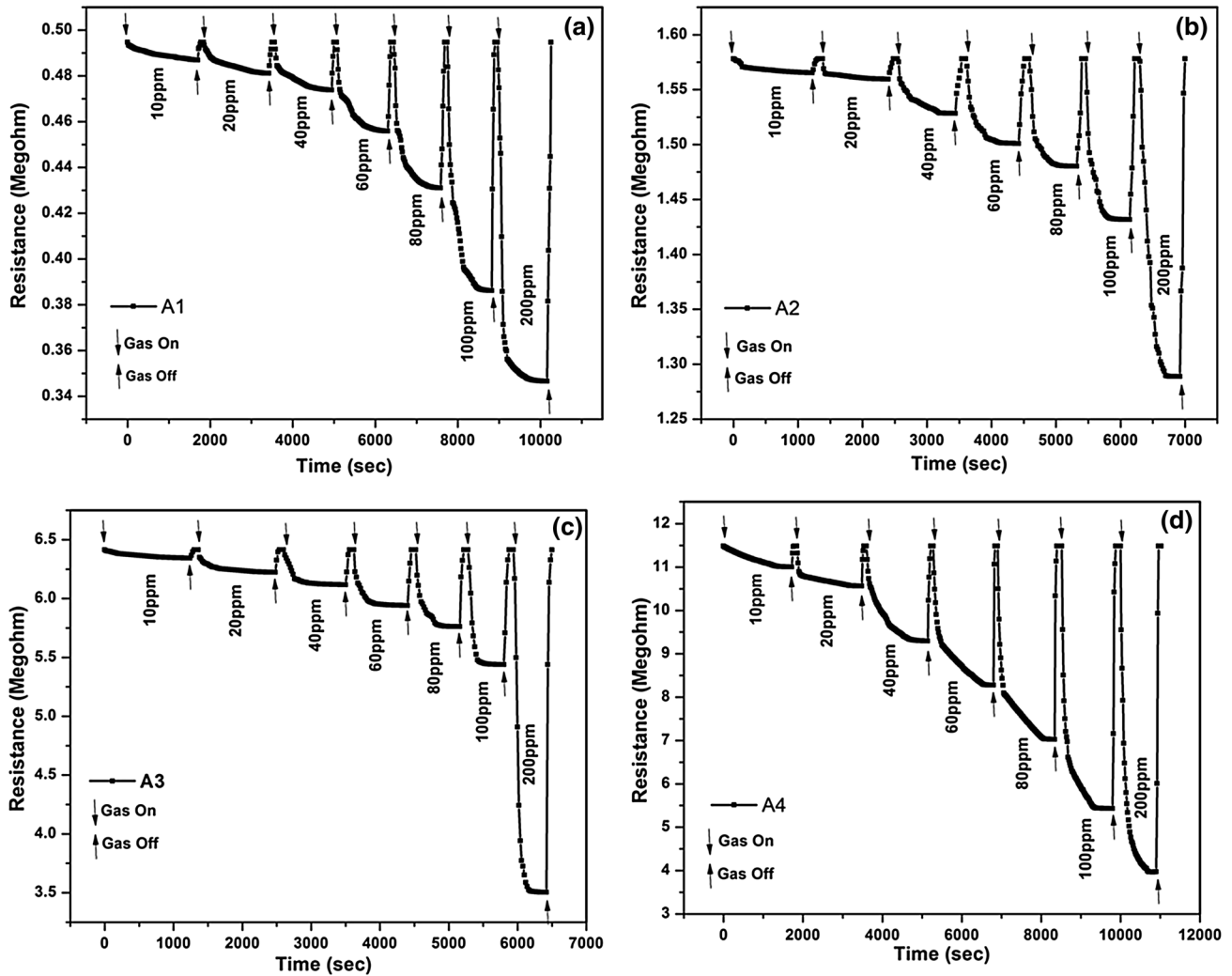


Fig. 5 a–d Variation in sensor resistance as a function of time and gas concentrations for different doping levels of Sn

When the minimum resistance R_g was achieved, dry air is supplied till the film regains its resistance value equal to R_a and thus one cycle of sensing process gets completed. The resistance values are recorded at regular intervals of time (10 s) starting from the time of injection of the test gas.

This process is repeated for various gas concentration levels viz. 10, 20, 40, 60, 80, 100 and 200 ppm. Using these curves (Fig. 5a–d), sensor response and recovery times can be calculated from the electrical resistance values R_a and R_g using the Eqs. (7) and (8) [27]

$$\text{Response time } (t_{Res}) = (t_{Ra} \sim t_{Rg}) \times 90/100 \tag{7}$$

$$\text{Recovery time } (t_{Rec}) = (t_{Ra} \sim t_{Rg}) \times 10/100 \tag{8}$$

The calculated response and recovery times of all the four samples are given in Table 2. It is observed that the

response time for the first three samples decreases when the concentration of ammonia gas increases (Fig. 6 a, b) whereas the response time increases for the sample A4 (Sn 8 at.%). This increase in response time for the sample A4 may be due to the agglomerations of crystals and the consequent decrease in the adsorption of oxygen on the surface.

A similar decreasing trend is observed for recovery time also (Fig. 6b), which may be due to the adsorption of a number of oxygen molecules from the dry air. However, for the sample A4 an increase in recovery time was observed.

Figure 7b shows the sensor response of all the films. The slope of the curve for the samples A1 to A4 increases gradually. The slope of A4 is found to be maximum when compared with other samples, but the resistance of the sensor reaches saturation quickly and remains constant as the concentration increases till 200 ppm. The response and recovery time of A4 is larger than those of A3, as seen from the

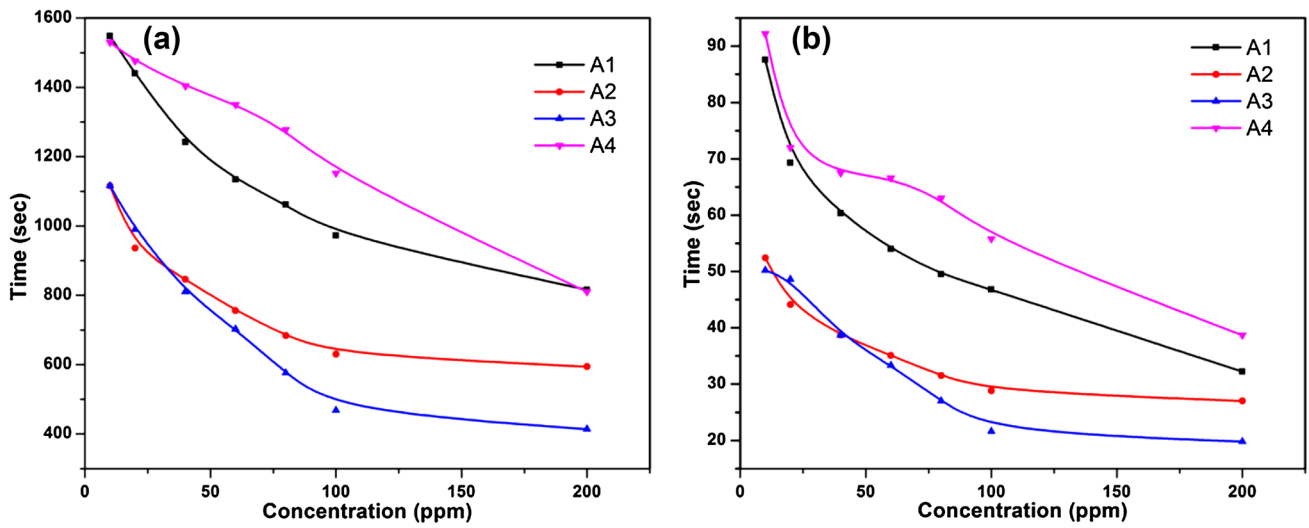


Fig. 6 Sensor response time (a) and recovery time (b) versus gas concentration

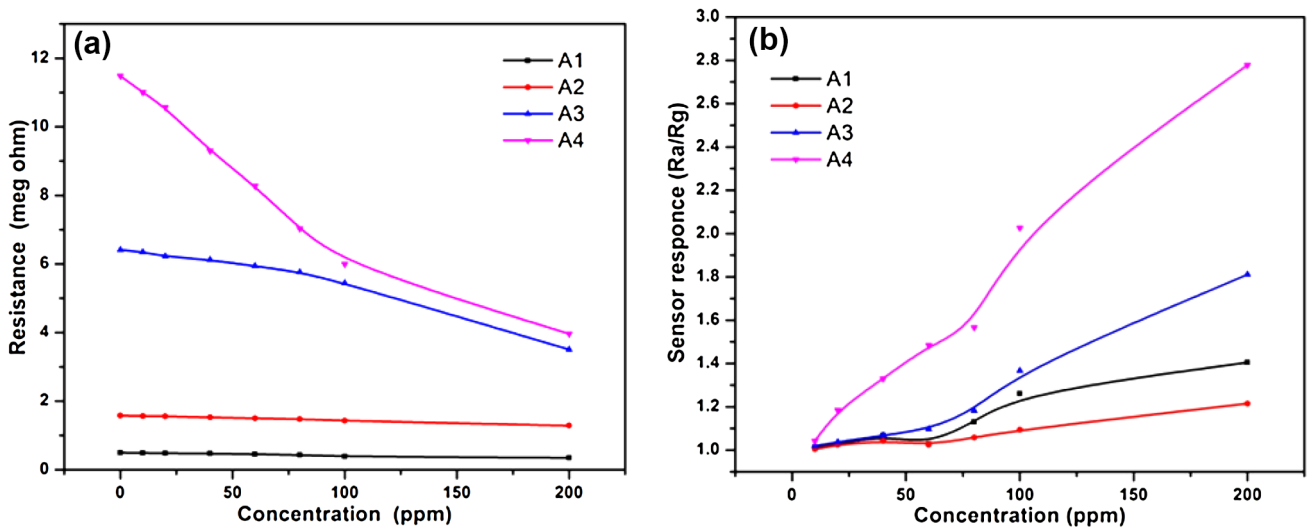


Fig. 7 Sensor resistance versus gas concentration (a) and sensor response ratio versus gas concentration (b) plots

Table 4 The response time and recovery time of the TZO sensor

Concentration (ppm)	Response time (s)				Recovery time (s)			
	A1	A2	A3	A4	A1	A2	A3	A4
10	1548	1116	1116	1530	58	32	34	52
20	1440	936	990	1476	69	47	48	72
40	1242	846	810	1404	60	39	36	68
60	1134	756	702	1350	54	35	33	67
80	1062	684	576	1278	49	31	27	63
100	972	630	468	1152	47	28	21	55
200	1116	594	414	810	52	27	19	38

Table 4. From the PL spectra, it is observed that the deficiency of oxygen for A4 is lesser than that for A3, which supports the above discussion.

The adsorption and desorption of target gas molecules on the surface of the prepared Sn doped ZnO films cause changes in the resistance of the materials. On exposing the TZO samples to air, interaction of the surface with the oxygen molecules results in the capturing of electrons from the conduction band of ZnO which in turn leads to a decrease in the resistance [28]. When the film is exposed to ammonia gas, the NH_3 molecules react with the existing oxygen ion, and facilitate the release of electrons into the conduction band [29]. Therefore, the resistance decreases. The large number of active sites for oxygen on the surface of the sensor materials plays a key role in the enhancement of gas sensing ability of the material [30, 31]. In the present work, the incorporation of Sn into the ZnO lattice offers relatively larger number of active sites and thereby improves the sensitivity of the films.

3.3 Surface morphology

Figure 8 shows FESEM images of the TZO samples recorded with same magnification. It is observed from the images that the changes in grain size and creation of topographical defects strongly depend upon the doping

level of tin. It is obvious from the Fig. 8 that when the doping concentration of tin is increased from 2 to 6 at.%, the pores on the surface increase (Fig. 8A3). This supports the sensing behavior of this sample. It is well known that porosity is one of the main factors that determine the sensing behavior of thin films. When the deposited film is subjected to gas sensing study, only the top surface which is exposed to gas will take part in the gas sensing process. If the sample has pores on its surface, the contour surfaces also take part in sensing a gas and consequently enhances the gas sensitivity of the sample. In other words, the surface with high porosity results in better sensitivity against any gas.

AFM images are shown in Fig. 9, which strongly support the discussed sensing behavior of the samples. AFM measurements were carried out for all the samples over the surface area of $100 \mu\text{m}^2$. Strong differences between the samples were observed as doping percentage of Sn increases. The average roughness (R_a) and RMS of roughness (R_q) found to increase as Sn doping concentration increases in the samples as given in Table 5. This increase in roughness creates more effective surface area to trap oxygen from the air [32]. The highest values of R_q and R_a observed for the sample A3 supports the discussion about the porosity of the film given in FESEM studies.

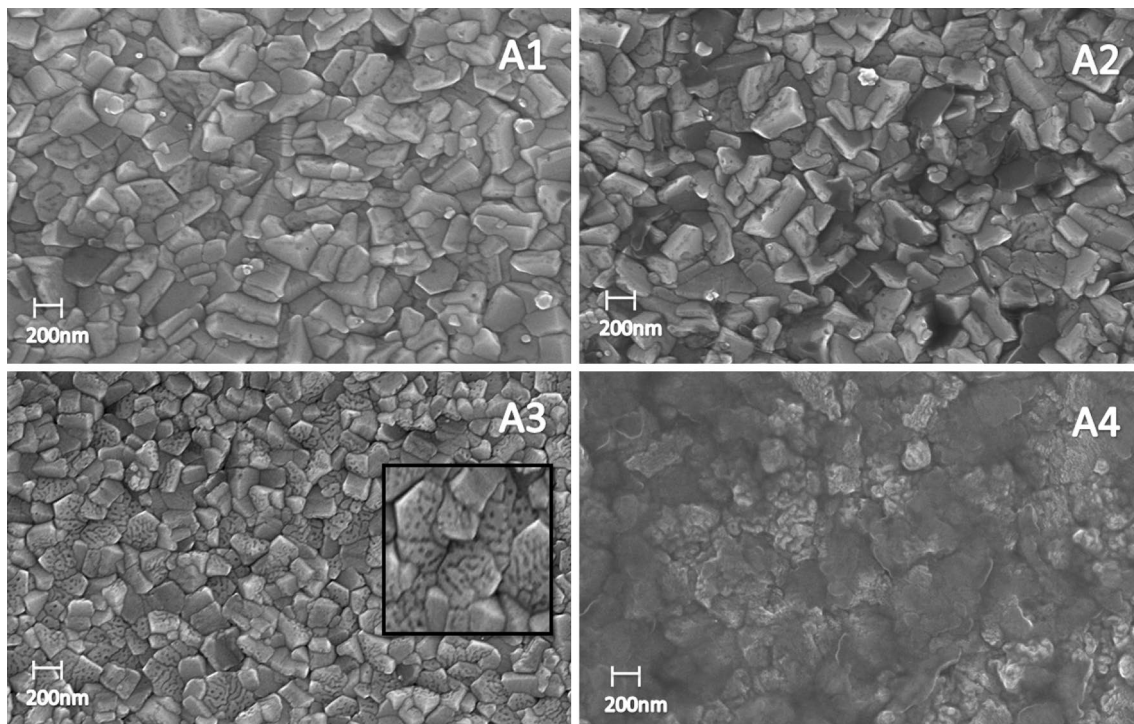


Fig. 8 FESEM images of TZO films. *Inset* in A3 (enlarged portion) shows the porous nature of the film

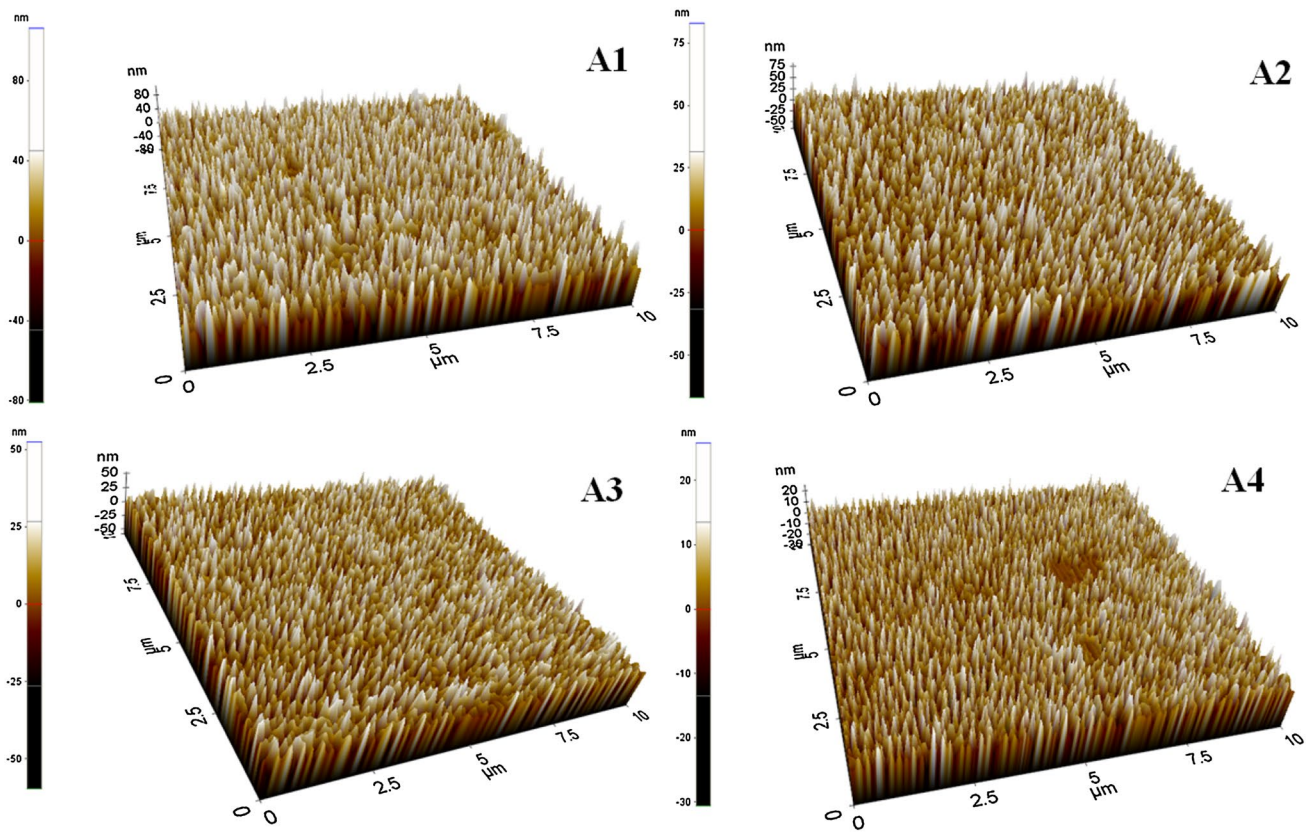


Fig. 9 AFM images of TZO films

Table 5 Roughness parameters of TZO thin films

Sn doping level at. %	Name of the sample	Axis	R_q (nm)	R_a (nm)
2	A1	X	17.496	14.026
		Y	13.569	10.543
4	A2	X	7.002	5.612
		Y	6.988	5.417
6	A3	X	20.743	17.515
		Y	21.138	16.352
8	A4	X	17.582	14.614
		Y	14.319	11.384

3.4 Photoluminescence studies

Figure 10 shows the photoluminescence spectra of TZO samples. The strong peak around 390 nm (UV emission) is an evidence for the crystalline quality of the films [33]. When the Sn doping level increases, the NBE peak shifts towards red. The peaks at 425 and 468 nm correspond to the defect level emissions are related to the zinc interstitials

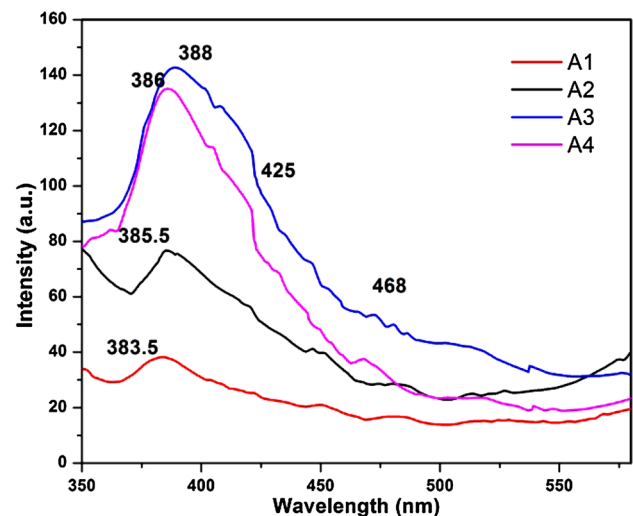


Fig. 10 PL spectra of TZO films

and singly ionized oxygen vacancies, respectively [34, 35]. Comparing all the samples, the one with doping level 6 at. % is found to have a maximum number of singly ionized oxygen vacancies which indicates that it can be able to attract more ammonia gas molecules.

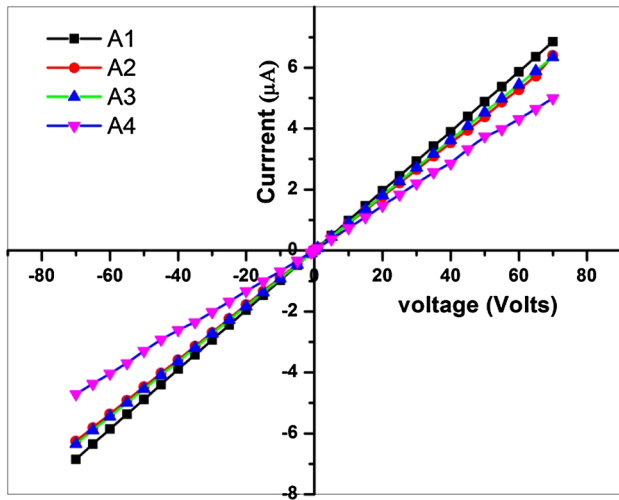


Fig. 11 I–V curves of TZO films

3.5 Electrical studies

I-V curves of the samples are shown in Fig. 11. From the figure, it is observed that the increase in Sn percentage increases the resistance of the corresponding samples, due to the maximum lattice distortion caused by the dopant. The observed I–V curves show the well established ohmic variations of all the samples.

3.6 Optical studies

Figure 12a shows the optical transmittance spectra of TZO films in the wavelength range of 300 to 1100 nm. The spectra show that when the Sn doping concentration increases,

the transmittance increases. All the films have high average transmission above 80% in the visible region. This high transmission is attributed to low scattering effect owing to the structural homogeneity and high crystalline quality of the films [36]. A sharp fundamental absorption is observed for at ~380 nm all the films which correspond to the transitions of electrons from valence band to conduction band. The transmittance decreases in IR region for all the films which is due to IR scattering caused by the excess of charge carriers generated by Sn doping [37]. This is a supplementary evidence for the successful substitution of Zn²⁺ ions by Sn⁴⁺ ions.

The optical band gap of the films is calculated with the help of plots drawn between the first derivative of the transmittance with respect to the wavelength (dT/dλ) and energy (Fig. 12b) [38]. The band gap value is 3.35 eV for 2 at.% of Sn doping. The band gap decreases for further increase in Sn doping concentration. This decrease in the band gap may be due to band shrinkage effect (also called band gap renormalization/band gap narrowing) [39].

4 Conclusion

The ammonia gas sensing studies of Sn doped ZnO films reveal that Sn doping remarkably improves the gas sensing properties of ZnO films. Among the four different Sn doping concentrations examined (2, 4, 6 and 8 at.%), 6 at.% exhibits the best response and recovery for ammonia gas sensing. The FESEM studies show that the surface roughness as well as the grain size strongly influence the sensing properties of the ZnO:Sn films. The structural and

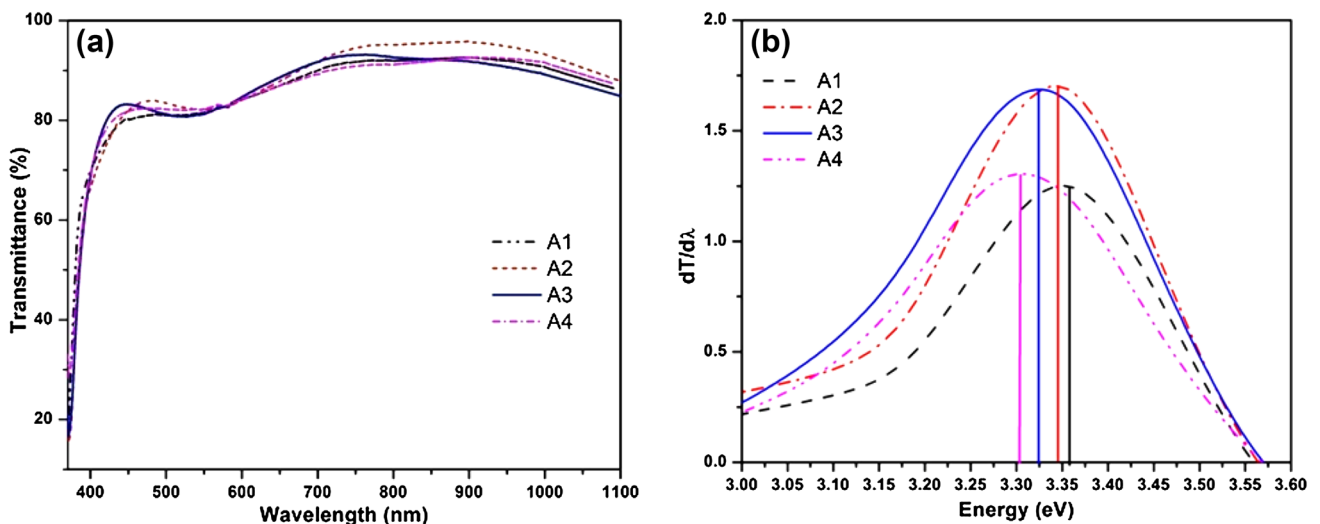


Fig. 12 a, b Transmittance spectra and dT/dλ vs energy plots of TZO films

photoluminescence studies support the major conclusions arrived at on the sensing properties of the prepared films.

References

1. C. Malins, A. Doyle, B.D. MacCraith, F. Kvasnik, M. Landl, P. Simon, *J. Environ. Monit.* **1**, 417–422 (1999)
2. V. Srivastava, K. Jain, *RSC Adv.* **5**, 56993–56997, (2015)
3. K. Wetchakun, T. Samerjai, N. Tamaekong, C. Liewhiran, C. Siriwong, V. Kruefu, A. Wisitsoraat, A. Tuantranont, S. Phanichphant, *Sens. Actuators B* **160**, 580–591 (2011)
4. H. Nanto, T. Minami, S. Takata, *J. Appl. Phys.* **60**, 482 (1986). doi:10.1063/1.337435
5. U. Özgür, Y.I. Alivov, C. Liu, A. Teke, M.A. Reshchikov, S. Doğan, *J. Appl. Phys.* **98**, 041301 (2005)
6. B. Timmer, W. Olthuis, A. van den Berg, *Sens. Actuators B* **107**, 666–677, (2005)
7. G. Mani, J. Rayappan, *Mater. Sci. Eng. B* **191**, 41–50 (2015)
8. C. Wang, L. Yin, L. Zhang, D. Xiang, R. Gao, *Sensors* **10**, 2088–2106 (2010)
9. T.P. Prasada Rao, M.C. Santhosh Kumar, A. Safarulla, V. Ganesan, S.R. Barman, C. Sanjeeviraja, *Physica B* **405**, 2226–2231 (2010)
10. M. Ajili, C. Michel, N. Turki, *Superlattices Microstruct.* **53**, 213–222 (2013)
11. K. Ravichandran, A. Anbazhagan, N. Dineshbabu, C. Ravidhas, *J. Mater. Sci.* **26**, 7649–7654 (2015)
12. R. Sridhar, C. Manoharan, S. Ramalingam, S. Dhanapandian, M. Bououdina, *Spectrochim. Acta Mol. Biomol. Spectrosc.* **120**, 297–303 (2014)
13. I. Akyuz, S. Kose, F. Atay, V. Bilgin, *Semicond. Sci. Technol.* **21**, 1620–1626 (2006)
14. Y. Kashiwaba, F. Katahira, K. Haga, T. Sekiguchi, H. Watanabe, *J. Cryst. Growth* **221**, 431–434 (2000)
15. G. Poongodi, P. Anandan, R. Mohan Kumar, R. Jayavel, *Spectrochim Acta A Mol. Biomol. Spectrosc.* **148**, 237–243 (2015)
16. A. Aravind, M.K. Jayaraj, M. Kumar, R. Chandra, *Appl. Surf. Sci.* **286**, 54–60 (2013)
17. K. Ravichandran, K. Subha, N. Dineshbabu, A. Manivasaham, *J. Alloys Compd.* **656**, 332–338 (2016)
18. S. Valanarasu, R. Chandramohan, *J. Alloys Compd.* **494**, 434–438 (2010)
19. R. Mariappan, V. Ponnuswamy, A. Chandra Bose, A. Chithambararaj, R. Suresh, M. Ragavendar, *Superlattices Microstruct.* **65**, 184–194 (2014)
20. S.T. Shishiyanu, T.S. Shishiyanu, O.I. Lupan, *Sens. Actuators B* **107**, 379–386 (2005)
21. A.K. Mukhopadhyay, P. Mitra, A.P. Chatterjee, H.S. Maiti, *Ceram. Int.* **26**, 123–132 (2000)
22. T. Sung, Y. Lo *Sens. Actuators B* **188**, 702–708 (2013)
23. A.P. Ramu, D. Sirbu, N. Iftimie, G.I. Rusu, *Thin Solid Films* **520**, 1303–1307 (2011)
24. K. Ravichandran, A. Manivasaham, K. Subha, A. Chandrabose, R. Mariappan, *Surf. Interfaces* **1–3**, 13–20 (2016)
25. R. Pandeewari, B. G. Jayaprakash, *Sens. Actuators B* **195**, 206–214 (2014)
26. C. Klingshirm, J. Fallert, H. Zhou, J. Sartor, C. Thiele, *Phys. Status Solid.* **247**, 1424–1447 (2010)
27. C.-Y. Tsay, H.-C. Cheng, Y.-T. Tung, Wei-H. Tuan, C.-K. Lin, *Thin Solid Films* **517**, 1032–1036 (2008)
28. V. Srivastava, K. Jain, *Sens. Actuators B.* **133**, 46–52 (2008)
29. K. Ravichandran, N. Dineshbabu, T. Arun, A. Manivasaham, E. Sindhuja, *Appl. Surf. Sci.* **392**, 624–633 (2017)
30. K. Ravichandran, R. Mohan, N. Jabena Begum, S. Snega, K. Swaminathan, C. Ravidhas, B. Sakthivel, S. Varadharajaperumal, *Vacuum* **107**, 68–76 (2014)
31. M. Benhaliliba, C.E. Benouis, Z. Mouffak, Y.S. Ocaik, A. Tiburcio-Silver, M.S. Aida, *Superlattices Microstruct.* **63**, 228–239 (2013)
32. N.L. Tarwal, K.V. Gurav, S.H. Mujawar, S.B. Sadale, K.W. Nam, W.R. Bae, A.V. Moholkar, J.H. Kim, P. S. Patil, J.H. Jang, *Ceram. Int.* **40**, 7669–7677 (2014)
33. R. Mariappan, V. Ponnuswamy, P. Suresh, *Superlattices Microstruct.* **52**, 500–513 (2012)
34. V. Jayaraman, A. Álvarez, O.M. de la Luzlvera Amador, *Materials Lett.* **157**, 169–171 (2015)
35. K. Ravichandran, P. Philominathan, *J. Mater. Sci.* **22**, 158–161 (2010)
36. Y. Caglar, S. Aksoya, S. Ilcan, M. Caglar, *Superlattices Microstruct.* **46**, 469–475 (2009)
37. S. Snega, K. Ravichandran, N. Jabena Begum, K. Thirumurugan, *J. Mater. Sci.* **24**, 135–141 (2013)
38. K. Ravichandran, K. Karthika, M. Baneto, K. Shanthakumari, K.C. Lalithambika, *J. Mater. Sci.* **26**, 1812–1819 (2015)
39. F.Z. Bedia, A. Bedia, N. Maloufi, M. Aillerie, F. Genty, B. Benyoucef, *J. Alloys Compd.* **616**, 312–318 (2014)